

Article

# Photocatalytic BiOX Mortars under Visible Light Irradiation: Compatibility, NO<sub>x</sub> Efficiency and Nitrate Selectivity

Magaly Y. Nava-Núñez <sup>1</sup>, Eva Jimenez-Relinque <sup>2,\*</sup>, Maria Grande <sup>2</sup>,  
Azael Martínez-de la Cruz <sup>2</sup>  and Marta Castellote <sup>2,\*</sup>

<sup>1</sup> CIIDIT, Facultad de Ingeniería Mecánica y Eléctrica, Universidad Autónoma de Nuevo León, Ciudad Universitaria, C.P. San Nicolás de los Garza 66451, Mexico; magaly.navanu@uanl.edu.mx

<sup>2</sup> Eduardo Torroja Institute of Construction Sciences, IETcc, CSIC, Serrano Galvache 4, 28033 Madrid, Spain; M.grande@ietcc.csic.es (M.G.); azael.martinezdl@uanl.edu.mx (A.M.-d.l.C.)

\* Correspondence: eva.jimenez@csic.es (E.J.-R.); Martaca@ietcc.csic.es (M.C.)

Received: 16 January 2020; Accepted: 6 February 2020; Published: 14 February 2020



**Abstract:** The use of new photocatalysts active under visible light in cement-based building materials represents one interesting alternative to improve the air quality in the urban areas. This work undertakes the feasibility of using BiOX (X = Cl and I) as an addition on mortars for visible-light-driven NO<sub>x</sub> removal. The interaction between BiOX photocatalysts and cement matrix, and the influence of their addition on the inherent properties of the cement-based materials was studied. The NO removal by the samples ranking as follows BiOCl-cem > BiOI-cem > TiO<sub>2</sub>-cem. The higher efficiency under visible light of BiOCl-cem might be ascribed to the presence of oxygen vacancies together with a strong oxidation potential. BiOI-cem suffers a phase transformation of BiOI in alkaline media to an I-deficient bismuth oxide compound with poor visible light absorbance capability. However, BiOI-cem showed considerably higher nitrate selectivity that resulted in the highest NO<sub>x</sub> global removal efficiency. These results can make its use more environmentally sustainable than TiO<sub>2</sub> and BiOCl cement composites.

**Keywords:** BiOI; BiOCl; visible; photocatalysis; cement; NO<sub>x</sub>; selectivity

## 1. Introduction

Photocatalytic building materials show diverse properties, such as the decomposition of air contaminants, as well as self-cleaning, antifogging, and self-disinfection [1–6]. Among them, the removal of nitrogen oxides (NO<sub>x</sub>) for air purification is the most extensively studied application due to urgent demand for technologies to reduce urban pollution from vehicle gaseous exhaust emissions [7,8].

The interest in combining the use of photocatalysts with construction materials has promoted its application in a wide variety of building materials as supporting media, such as cement mortar, tiles, paving blocks, glass, and PVC fabric [1]. Among them, cementitious materials are the most widely used due to their strong binding property and porous structure [2]. Generally, the photocatalyst is loaded or mixed with cementitious material. When the photocatalyst is exposed to solar light, it can absorb photon energy and promote electrons to jump from the valence (VB) to the conduction band (CB) of the semiconductor used producing (h<sup>+</sup>) and free electrons (e<sup>-</sup>), respectively. By migration of these generated species to the surface of the photocatalyst, in the presence of molecules of water and oxygen adsorbed, the formation of •OH and •O<sub>2</sub><sup>-</sup> radicals that can participate in redox reactions to eliminate molecules of pollutants adsorbed is possible.

Among the available photocatalysts, nano-sized titanium dioxide (TiO<sub>2</sub>) is the most widely used due to its chemical stability, good optical transparency, high refractive index, low cost, and non-chemical

toxicity. Nevertheless, the limited visible light absorption and high electron-hole recombination rate are considered the drawbacks of its wide application [9,10].

Recently, there has been considerable research interest in layered composite materials, such as silicates [11,12], graphene [13–16], perovskites [17], graphitic carbon nitrides [18,19] and layered double hydroxides [20]. These layered materials possess several extraordinary advantages, such as high surface area, more surface-active sites, superior electron mobility, and good electron transfer, endowing them with promising potential for photocatalytic applications. Of these layered materials, bismuth oxyhalides (BiOX, X = Cl, Br, and I) belong to a new class of promising layered materials because of their unique layered-structure-mediated fascinating physicochemical properties and suitable band-structure, as well as their high chemical and optical stability, nontoxicity, low cost, and corrosion resistance [21,22]. Among all of BiOX materials, BiOI with band gap energy of 1.7 eV exhibits the highest visible light-driven photocatalytic activity attributed to its smaller band gap [21,23,24]. Many studies have investigated the removal of nitric oxide gas-phase through pure BiOX photocatalysts, but most are focused on the performance based on the decrease of NO concentration [10,25–28]. Only a few reports focus on the final or by-products of NO removal process [9,23,29]. The mechanisms of NO removal remain unclear in the literature. Generally, NO can be oxidized by either photogenerated hole or other active species [30–32] to different kinds of products, such as NO<sub>2</sub>, HNO<sub>2</sub>, and HNO<sub>3</sub>. However, some of these products, such as NO<sub>2</sub>, is considerably more toxic than NO [31].

Moreover, very scarce references have been found in relation to the addition of BiOX oxides into construction materials. For example, Wang et al. [33] prepared cement-based materials with coatings of BiOBr with photocatalytic activity for the degradation of Rhodamine B and propylene. Mera et al. [28] prepared ceramic paints and stucco with additions of BiOI photocatalyst. However, this is focused on the activity of photocatalyst composites based only on the decrease of NO concentration. Few reports are available about the bonding and interactions between bismuth-based photocatalysts and cement matrices, and the effects on the inherent properties of the cement-based materials.

In this context, this paper shows the results of the influence of bismuth-based photocatalysts (BiOI and BiOCl) addition to mortars on the inherent properties of the cement-based materials, and the interaction between BiOX and the cement matrix. The pollutant removal ability of photocatalyst/cement samples under visible light was determined by the photocatalytic conversion rate of NO-NO<sub>x</sub> and selectivity to nitrates. The photocatalytic performance in the function of physicochemical and optical properties is critically discussed.

## 2. Results and Discussion

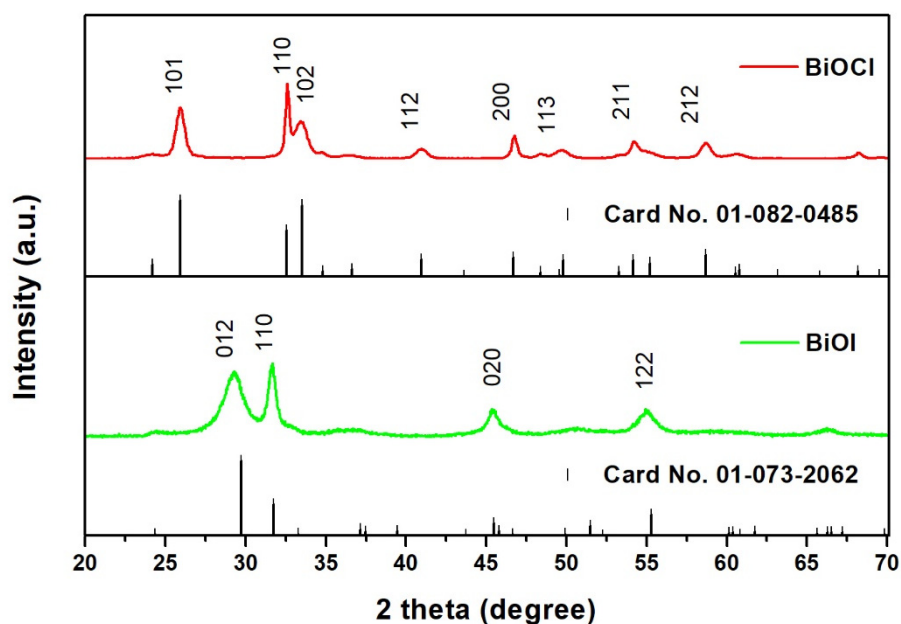
### 2.1. Physicochemical Characterization

#### 2.1.1. Photocatalysts

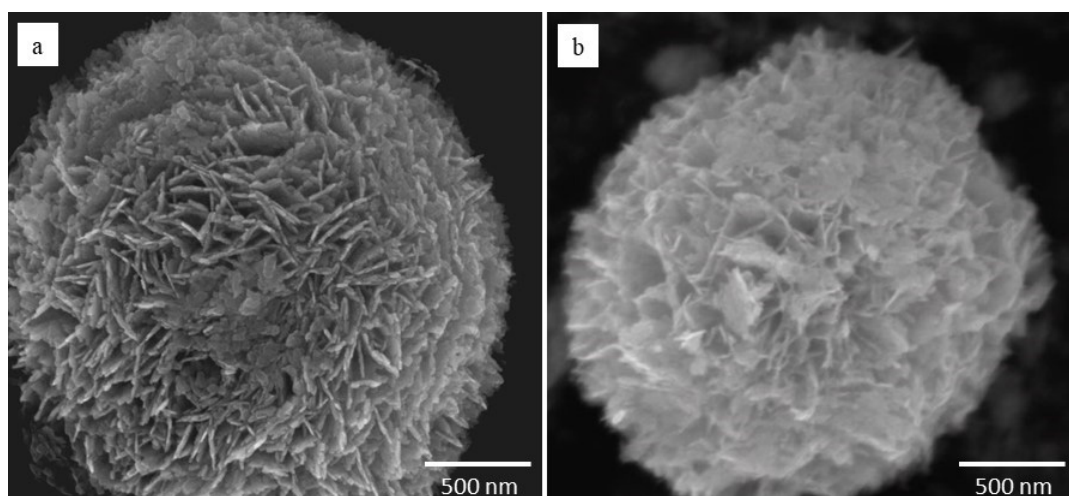
Figure 1 shows the diffraction patterns of both BiOX synthesized samples together with their reference cards (JCPDS card no. 01-082-0485 and 01-073-2062) for BiOCl and BiOI, respectively. No extra peaks were observed. The crystalline size from an analysis of the X-ray peak widths using the Scherrer equation was found to be  $8 \pm 3$  nm for BiOI and  $12 \pm 4$  nm for BiOCl. [34,35]. The grain size is consistent with previous reports [36,37]. The scatter between reported values may be related with some peaks indexed were not resolved properly.

Figure 2 shows representative SEM images of the BiOX oxides, where different morphology can be appreciated in the samples. SEM images of BiOCl and BiOI show that the particles are of a spherical shape with a flower-like morphology. The size of spheres for BiOCl is a bit higher than for BiOI, with average diameters of  $2 \pm 0.5$   $\mu$ m and 1 to 1.5  $\mu$ m, respectively. The spheres are composed of nanosheets as elementary units differently packed in both compounds. In the case of BiOCl, the nanosheets have a thickness of 10 to 20 nm and are densely packed as petals of a flower, which assembled to form a single flower structure. BiOI oxide presented a similar morphology, but the nanosheets are not so tightly packed and are thinner (around 5 nm) than in the case of BiOCl

samples. Micrometric size can reduce the possible environmental risk associated with the use of nanoparticle formulations.



**Figure 1.** XRD diffraction pattern of BiOCl and BiOI photocatalysts.



**Figure 2.** SEM images of the as synthesized (a) BiOCl sample by co-precipitation, and (b) BiOI sample by microwave method.

In the case of sedimentation tests (Figure 3), neither of the three dispersions was stable in the synthetic alkaline pore solution. When suspended fresh photocatalysts in the solution, before 1 min, the samples of BiOCl and BiOI showed significant sediment, more compact in the case of BiOCl. After 3 min, TiO<sub>2</sub> started to sediment, leaving a clear border between the liquid and the solid phase. From the supernatant solutions and the volume of the precipitate of sediment test images (Figure 3), some observations can be also derived [38,39]. BiOCl formed a compact precipitate that did not change appreciably in volume with time, leaving a supernatant solution that does not appear totally clear at 35 min. The opposite behavior is presented by TiO<sub>2</sub>, with a kind of slow sediment that reduces its volume with time leaving a clear supernatant liquid. According to [39], the volume of the sediment decreases in time due to rearrangements caused by gravity, and the supernatant solution appears

clearer at any time because the bigger aggregates are less affected by thermal motion. This may imply that  $\text{TiO}_2$  forms flocculated sediment while  $\text{BiOCl}$  forms a deflocculated sediment, due to its larger elemental particle size.  $\text{BiOI}$  presents an intermediate behavior, with the remarkable aspect that the color of the sample changes significantly to a yellowish lighter color, which can be indicative of an interaction with the alkaline aqueous phase of the cement like-pore synthetic solution. The color change to yellow was also observed in previous works [40,41].

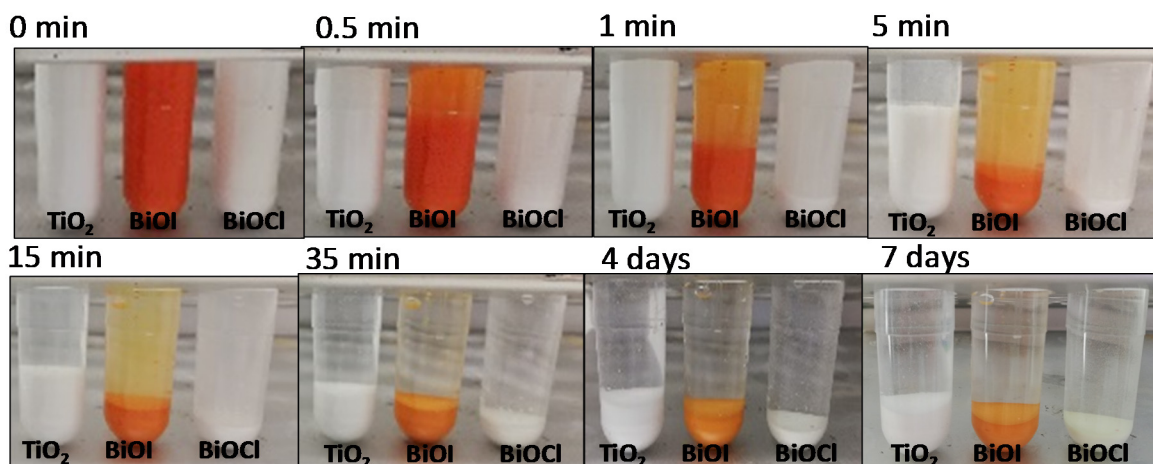


Figure 3. Sedimentation test for photocatalysts in the synthetic cement-pore solution.

To confirm the interaction between the alkaline solution and bismuth oxyiodide, the XRD patterns of  $\text{BiOI}$  photocatalyst powder before and after two weeks of contact with the synthetic cement-pore solution (named as  $\text{BiOI-pore}$ ) are depicted in Figure 4. As a result, some features were observed. In the first instance, the position and intensity of the diffraction lines were modified. The characteristic peak of  $\text{BiOI}$  for the 110-plane decreased significantly, and peaks corresponding to  $\text{Bi}_2\text{O}_3$  and  $\text{Bi}_5\text{O}_7\text{I}$  in the  $\text{BiOI-pore}$  sample appeared [40–42]. The transformation of  $\text{BiOI}$  in these I-deficient bismuth oxyiodide compounds in alkaline pH conditions is consistent with previous reports [41,43]. The transformation of  $\text{BiOI}$  in  $\text{Bi}_5\text{O}_7\text{I}$  due to alkali media and heating has been reported by other authors [44].

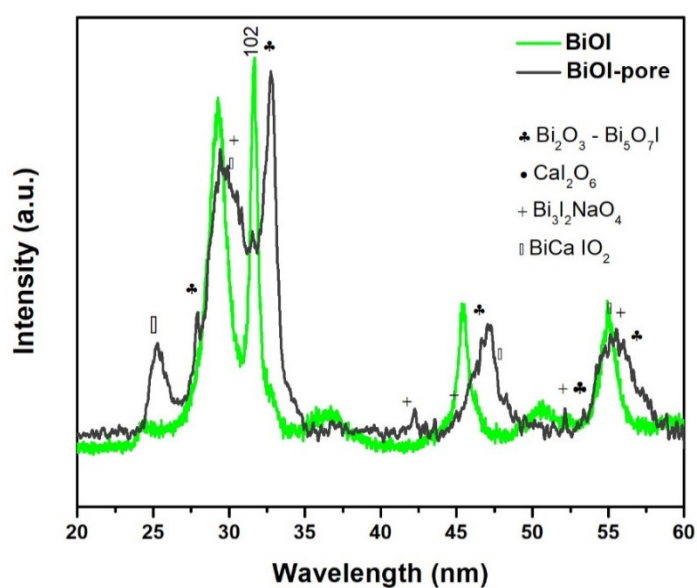


Figure 4. XRD pattern of  $\text{BiOI}$  photocatalyst before and after two weeks of contact with alkaline pH synthetic cement-pore solution ( $\text{BiOI-pore}$ ).

Furthermore, other peaks of some interactions between cationic ions ( $\text{Ca}^{2+}$  and  $\text{Na}^+$ ) of cement-like pore solution with BiOI photocatalyst were identified as  $\text{CaI}_2\text{O}_6$ ,  $\text{Bi}_3\text{I}_2\text{NaO}_4$ , and  $\text{BiCaIO}_2$ . These results indicated that this partial transformation of BiOI is likely to occur also in aqueous pores of cementitious matrixes.

Nitrogen adsorption-desorption isotherms for the three photocatalysts are shown in Figure 5a. BiOX photocatalysts have BET curves of type IV, which is typical of a material with pore-size distribution in the mesoporous region [23].  $\text{TiO}_2$  isotherm presents a shape type II, which reveals the non-porous character of the  $\text{TiO}_2$  nanoparticles. The shape of the hysteresis loops for the BiOX samples is categorized as type H3, which implies the formation of slit-like pores owing to the aggregation of the sheet-like particles [23,45]. The calculated BET surface areas ( $S_{\text{BET}}$ ) of BiOCl, BiOI, and  $\text{TiO}_2$  samples were about 40, 57, and 50  $\text{m}^2/\text{g}$ , respectively. Among the three pure photocatalyst samples, the  $S_{\text{BET}}$  of BiOI is relatively higher than the other ones, in agreement with their more open hierarchical flower-like microsphere architecture observed in SEM images (Figure 2). Figure 5b presents, for the BiOX powders, the differential distribution of the pores in the range 1–100 nm, presenting both samples a maximum between 2 and 6 nm.

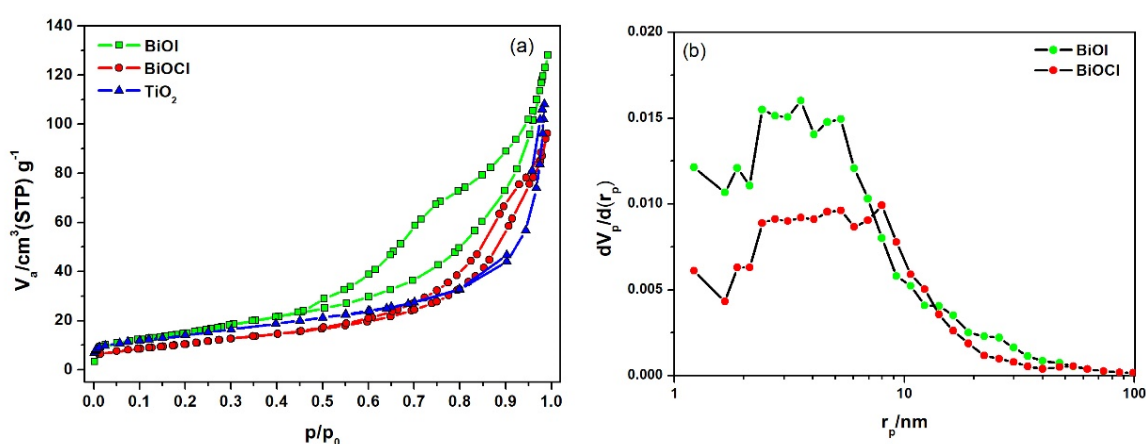


Figure 5. (a)  $\text{N}_2$  adsorption-desorption isotherms and (b) pore-size distribution curves of pure photocatalysts.

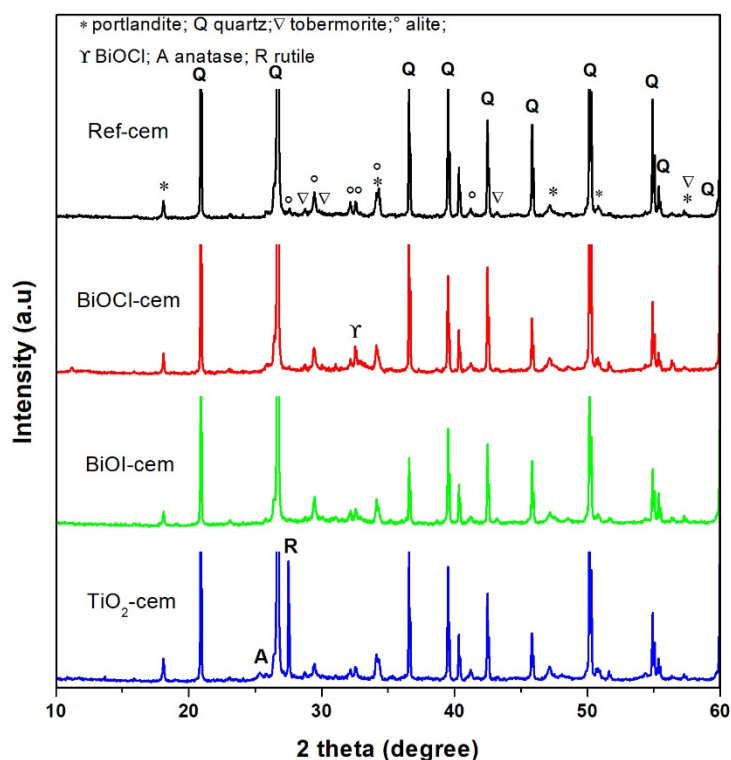
### 2.1.2. Cement-Based Materials

Table 1 shows the results of fresh characteristics, mechanical properties, and electrical resistivity of the mortars. The workability expressed as slump flow diameters of all mixtures was in the range of 117–180 mm and the density was in the range of 2110–2150  $\text{Kg}/\text{m}^2$ . Comparing the workability values, as already reported [2] the addition of  $\text{TiO}_2$  makes the mix more water demanding, which is the opposite effect of the incorporation of BiOI and BiOCl which can be attributed to the different particle size, acting  $\text{TiO}_2$ , finer than BiOX as a filler. Concerning density in fresh state, the incorporation of any catalyst increases it in comparison with the plain mortar. Concerning compressive strength, no significant changes could be observed due to the addition of the photocatalysts.

Table 1. Fresh, mechanical and electric resistivity properties of tested samples.

Samples	Workability	Density in	Compressive	Resistivity
	Diameter Slump	Fresh State	Strength (28 days)	(28 days)
	(mm)	( $\text{Kg}/\text{m}^3$ )	(MPa)	( $\text{K}\Omega\cdot\text{m}$ )
Ref-cem	138 ± 2	2110	38.42 ± 0.61	0.10 ± 0.00
BiOCl-cem	180 ± 3	2130	37.54 ± 1.00	0.07 ± 0.00
BiOI-cem	176 ± 6	2150	38.89 ± 0.30	0.11 ± 0.00
$\text{TiO}_2$ -cem	117 ± 0	2120	39.01 ± 0.66	0.11 ± 0.01

The XRD patterns of cement-based samples are depicted in Figure 6. A small amount of BiOCl could be identified in BiOCl-cem sample at 25.8°, 32.4°, and 33.2° (2 theta). For BiOI-cem, the phases corresponding to the photocatalyst could not be identified probably due to the high intensity of the quartz (SiO<sub>2</sub>) used as aggregate [46] that masks the smallest peaks. In the case of TiO<sub>2</sub>-cem, the peaks corresponding to anatase and rutile of Aeroxide® TiO<sub>2</sub>-P25 photocatalyst were detected.



**Figure 6.** XRD patterns of reference cement-based sample and photocatalyst/cement composites.

Figure 7 presents the graphs corresponding to the TGA/DTA trials for the different mortars. From these graphs, it is possible to measure the amount of evaporable water, C–S–H gel water, the portlandite, the CO<sub>2</sub> bound as calcium carbonate, as well as any other compounds coming from the photocatalysts that could decompose due to the thermal action. The evaporable water is lost up to 110 °C. The water lost from 110 °C to the beginning of portlandite decomposition, around 400 °C is named ‘C–S–H combined water’. Nevertheless, it is important to emphasize that this water does not comprise the total amount of C–S–H water, considering that the differences are within the range of the TGA technique accuracy [47]. The same procedure has been applied for the calculation of the amounts of portlandite and calcium carbonate, and the results are shown in Table 2.

From Figure 7 it can be noticed that BiOI-cem shown an additional peak around 725 °C followed by a more remarkable exothermic phenomenon that on Ref-cem sample which can be associated with the generation of new substance from the decomposition of BiOI photocatalyst. Previous work indicated that thermal stability BiOX is <525 °C (BiOI) and <675 °C (BiOCl) in air atmosphere [48]. Transformation of BiOI into Bi<sub>5</sub>O<sub>7</sub>I and Bi<sub>2</sub>O<sub>3</sub> from 600 to 850 with the release of I<sub>2</sub> around has been reported previously [44,48]. Provided that Bi<sub>5</sub>O<sub>7</sub>I is much more resistant to the hydrolysis in basic media than BiOI, and that Bi<sub>2</sub>O<sub>3</sub> are related in equilibrium with Bi<sub>5</sub>O<sub>7</sub>I, the peak that appears in the TG for BiOI-cem can be attributed to a mix of Bi<sub>5</sub>O<sub>7</sub>I and Bi<sub>2</sub>O<sub>3</sub> [43]. Thus, the decomposition of BiOI is not easy to be calculated as it is interfered with by other phases. The weight loss of BiOI considering a complete transformation of BiOI into Bi<sub>5</sub>O<sub>7</sub>I is about 8.32%. The values of quantities of the different phases coming from the cement are quite similar, not observing big differences between the different

mortars, being the most relevant aspect the smaller amount of portlandite of the sample BiOI-cem, maybe due to the uptake of  $\text{Ca}^+$  by the products of the reaction with BiOI (see Figure 4).

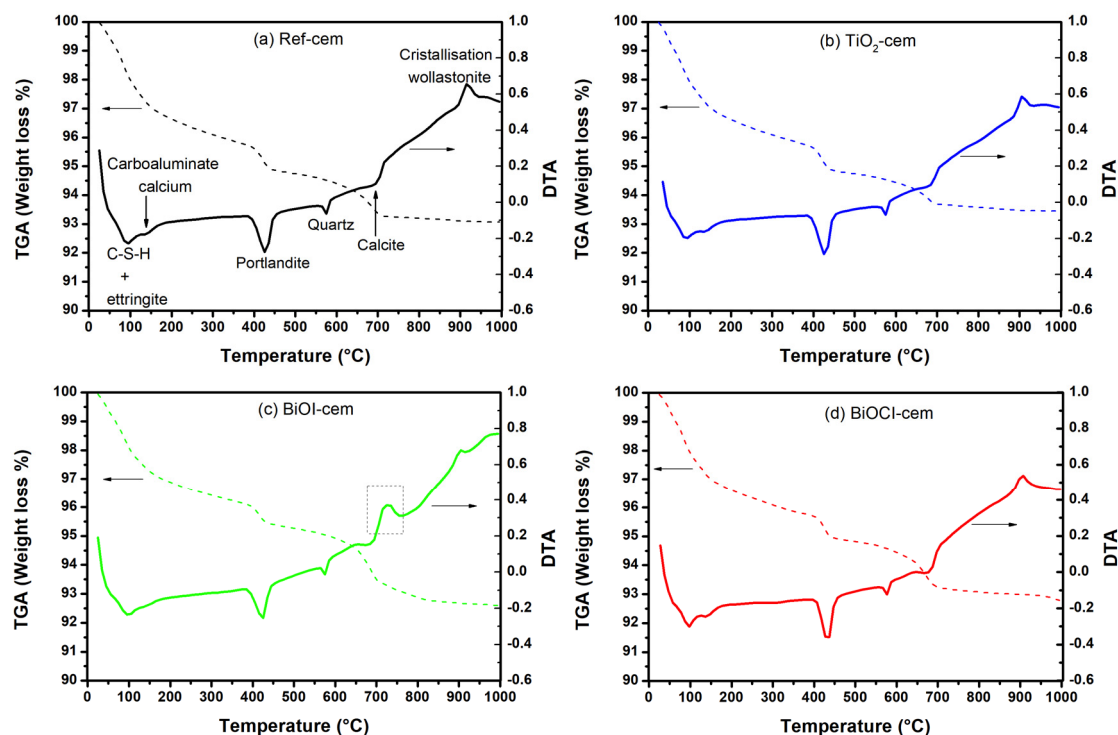


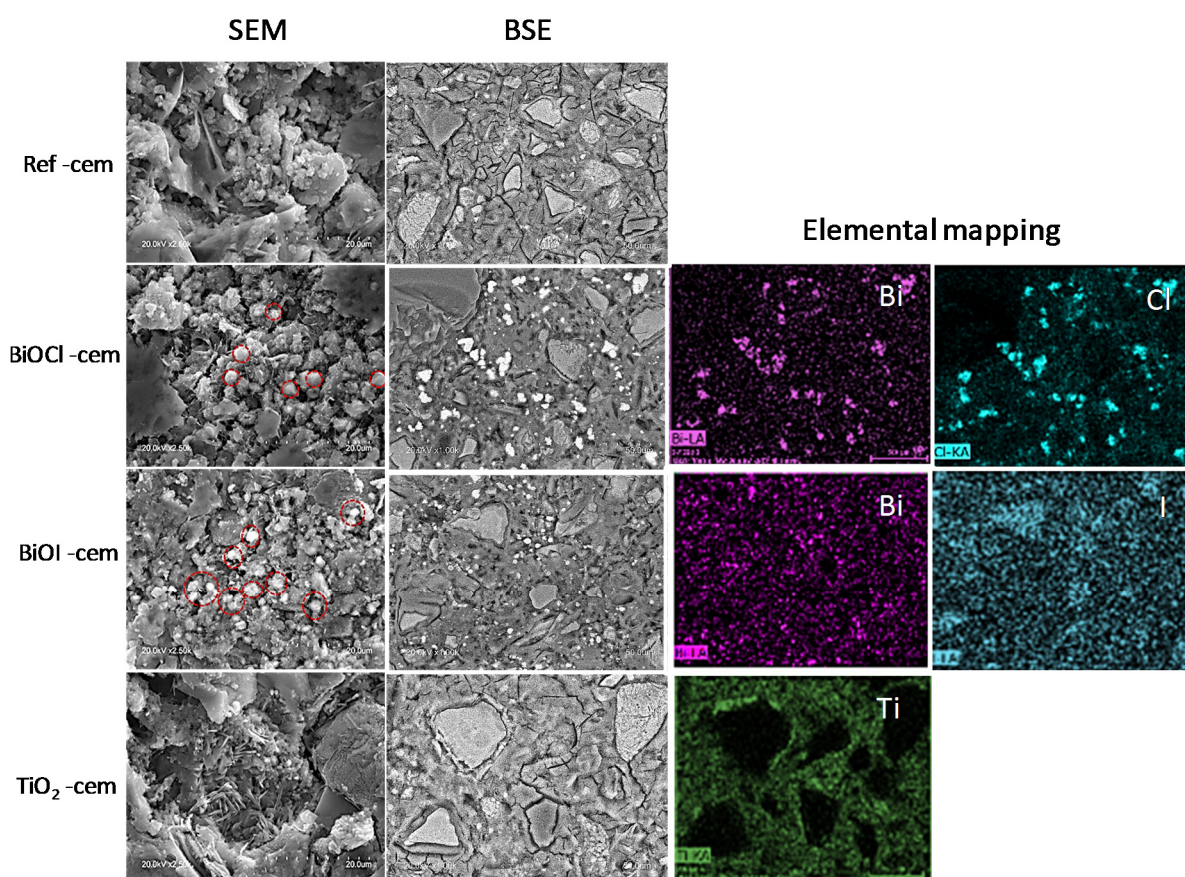
Figure 7. TGA results of reference cement-based sample and photocatalyst/cement composites.

Table 2. Weight loss (%) of compounds obtained by TGA in mortar samples.

	Ref-cem	TiO <sub>2</sub> -cem	BiOCl-cem	BiOI-cem
Free water	2.14	1.96	1.97	2.03
Bound water	2.61	2.74	2.81	2.47
Portlandite	2.55	2.71	2.10	1.60
Calcite	3.02	2.14	3.28	3.86
BiOI	-	-	-	8.32

Figure 8 shows SEM, BSE, and the corresponding elemental mapping images (Bi, Cl, I, and Ti) obtained for the different cement-based samples at the age of 28 days. TiO<sub>2</sub>-cem and Ref-cem samples present a drier aspect, with some microcracks, as it is a more water demanding mix (see BSE images in Figure 8). No cracks were observed in BiOX mortars, in agreement with their results of workability.

The BiOCl particles embedded in the matrix mortar were easily distinguishable in some specific areas due to their peculiar morphology (red circles in the SEM pictures). In BSE mode, they are visible as a bright agglomeration of particles, which is corroborated by mapping of Bi and Cl. Thus, particles of BiOCl were not distributed uniformly in the bulk of mortar, but in a flocculated manner with an agglomeration of particles, that can reach about 70  $\mu\text{m}$ . The same behavior took place for BiOI oxide containing mortars, with the difference that agglomerates were much smaller than those of BiOCl, and therefore it is better dispersed in the matrix, which is not in agreement with the sediment trials. Further research is needed to clarify this aspect. Additionally, the correspondence of Bi and I in the mapping is not so clear, finding I associated with the aggregates related with the dissociation or reaction of BiOI with some other component of the cement paste, in agreement with the formation of other phases in alkaline media. Figure 8 presents the images of TiO<sub>2</sub>-cem. It can be observed that TiO<sub>2</sub> is distributed homogeneously in the paste of the mortars, finding some more concentrated layers in the interphase with the aggregates.



**Figure 8.** SEM, BSE, and the corresponding elemental mapping images of reference and photocatalytic mortars at the age of 28 days. Red circles in SEM images corresponding with BiOX particles.

Table 3 shows the  $S_{BET}$  for the different mortars, being much higher in the case of adding the photocatalysts, especially for BiOX samples. The higher  $S_{BET}$  was obtained by BiOCl-cem followed by BiOI-cem,  $TiO_2$ -cem, and finally, the reference mortar. The results of MIP analysis are also given in Table 3, where it can be seen that even though the total porosity of the BiOX-cem samples is a bit higher than the other samples, no significant differences have been found.

**Table 3.** Brunauer–Emmett–Teller (BET) and mercury intrusion porosimetry (MIP) results of mortar tested samples.

Samples	$S_{BET}$ ( $m^2 g^{-1}$ )	Bulk Density * ( $g/mL$ )	Total Porosity * (% vol)
Ref-cem	4.7	2.12	14.3
BiOCl-cem	12.7	2.08	16.2
BiOI-cem	10.1	2.09	15.4
$TiO_2$ -cem	7.39	2.11	14.9

\* Results from MIP (range pores 0.01–100  $\mu m$ ).

A more detailed analysis can be performed by observing the accumulated and differential pore size distribution, as shown in Figure 9. The reference mortar presents a bimodal pattern, with maxima at around 0.2 and 1  $\mu m$ . This trend is maintained for the BiOX-cem, presenting some differences among them and with the reference. Both samples shifted the maxima corresponding to big pores toward bigger sizes (around 2  $\mu m$ ). Concerning the smaller pores, BiOCl increases its amount with a shift of the maxima to 0.1  $\mu m$  and a higher amount from 0.1–0.01  $\mu m$ . BiOI maintains the maximum at 0.2  $\mu m$  with a peak higher than the reference. The addition of  $TiO_2$  acts as a filler of higher pores leading to a refinement of the porosity, with a single-mode pore distribution towards smaller pores, encountering

a broad maximum at around smaller than 0.5  $\mu\text{m}$ . These results are in accordance with the BET specific surface area results mentioned above.

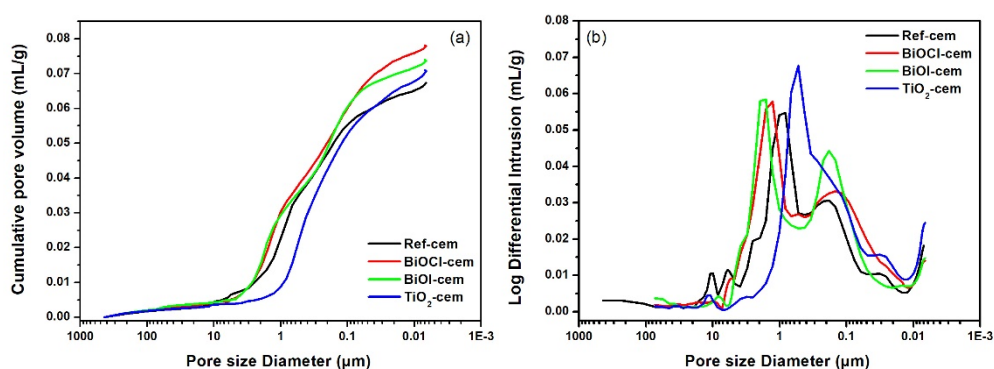


**Figure 9.** (a) Cumulative curves of the pore size distribution and (b) log differential intrusion with pore size diameter of the photocatalytic cement-based samples obtained by MIP.

## 2.2. Optical Properties

Figure 10a shows the UV–Vis DRS spectra of pure photocatalysts (including BiOI in the synthetic pore solution) and cement/photocatalyst specimens.  $\text{TiO}_2$  and BiOCl exhibit strong absorption in the ultraviolet region, and BiOI shows UV and visible-light absorption. A noticeable change in the absorption edges was observed in the UV region of the BiOI-pore sample due to previously explained phase transformation of BiOI into alkaline pH aqueous solutions. The cementitious mixture repeated the same behavior but with much lower values of light absorption intensity, see Figure 10b.

The  $E_g$  values of the pure catalysts samples could be thus estimated from the intercept of the tangent with the baseline absorption data from a plot of  $F(R)h\nu^{1/2}$  and  $F(R)h\nu^2$  versus the photon energy ( $h\nu$ ) for indirect and direct transitions, as shown in Figure 10c,d respectively [2] and [49].  $\text{TiO}_2$  and BiOCl have large band gap, while BiOI has a band gap of 1.93 eV (2.35 eV, direct transitions), which is suitable for visible-light excitation. BiOI-pore sample shift towards to 2.35 eV (see Table 4). The estimated band gap values of BiOX samples [21,23,29] and Aeroxide<sup>®</sup>  $\text{TiO}_2$  [46,50,51] are within the acceptable range previously reported. The scatter between reported values may be related with different micro/nanostructure and morphology of the semiconductors, which may modify the band gap as a result.

The conduction band ( $E_{CB}$ ) and valence band ( $E_{VB}$ ) potentials of BiOX photocatalysts samples at the point of zero charge (pHzpc) can be predicted by the equations (Equations (1) and (2)) [4,21]:

$$E_{CB} = \chi - E_C - 0.5E_g \quad (1)$$

$$E_{VB} = E_{CB} + E_g \quad (2)$$

where  $\chi$  is the absolute electronegativity of the semiconductor,  $E_C$  is the energy of free electrons on the hydrogen scale ( $\sim 4.5$  eV), and  $E_g$  is the band-gap energy of indirect and direct transitions of the semiconductor obtained by DRS measurements. The potential data of BiOX photocatalysts are listed in Table 4. The potential values of VB and CB of  $\text{TiO}_2$  were selected from our previous publication obtained by X-ray photoelectron spectroscopy [46].

According to this result, a schematic illustration of the band-gap structures for the photocatalyst samples can be drawn as is shown in Figure 11. The standard energy potentials for  $\text{O}_2/\bullet\text{O}_2^-$  ( $-0.33$  eV),  $\text{H}_2\text{O}/\bullet\text{OH}$  ( $+2.72$  eV) and  $\text{OH}^-/\bullet\text{OH}$  ( $+1.85$ – $2.00$  eV; pH = 12–14) have been also included.  $\text{TiO}_2$  and BiOCl are able to oxidize both  $\text{OH}^-/\text{H}_2\text{O}$  to  $\bullet\text{OH}$  by the photogenerated holes. However, BiOI is able to oxidize only the  $\text{OH}^-$  groups to  $\bullet\text{OH}$  radicals at alkaline pHs. The VB potential of BiOCl is 3.53 eV (3.70 eV, direct transitions), which means that it possesses strong oxidation ability. On the other hand, the VB potential of  $\text{TiO}_2$  and BiOI decreases to 2.80 and 2.46 eV (2.67 eV, direct

transitions) respectively, indicating that the oxidation ability of photogenerated holes is becoming poorer. The phase transformation of BiOI to I-deficient bismuth oxyiodide compounds into alkaline pH aqueous solutions (BiOI-pore) turns the VB potential to be much more positive than the precursor BiOI. Those findings are consistent with [44,52].

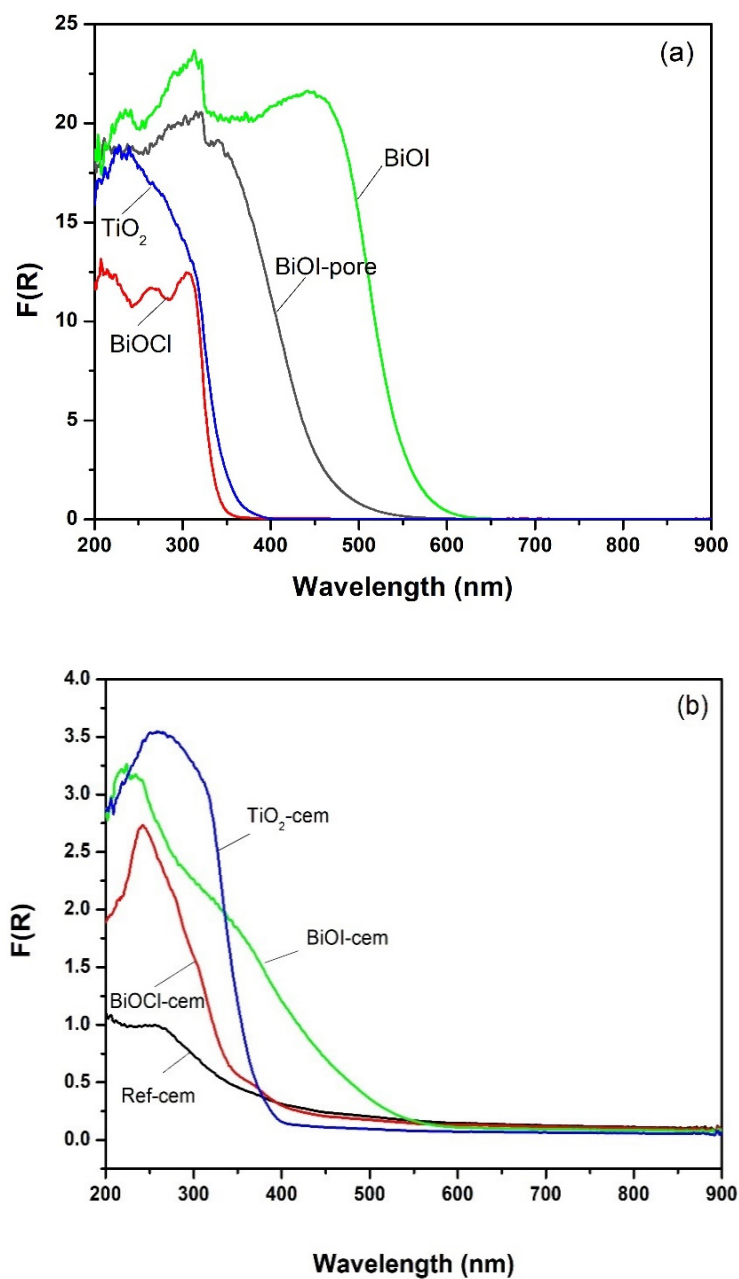
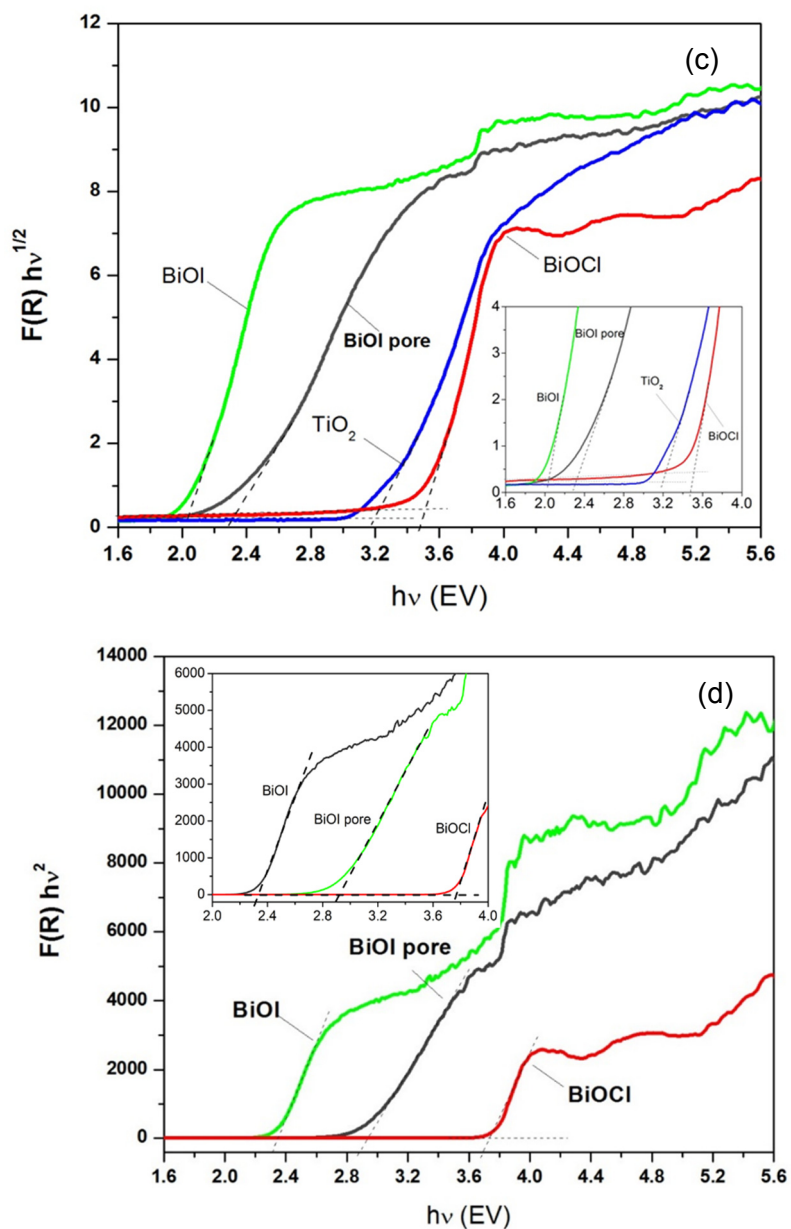
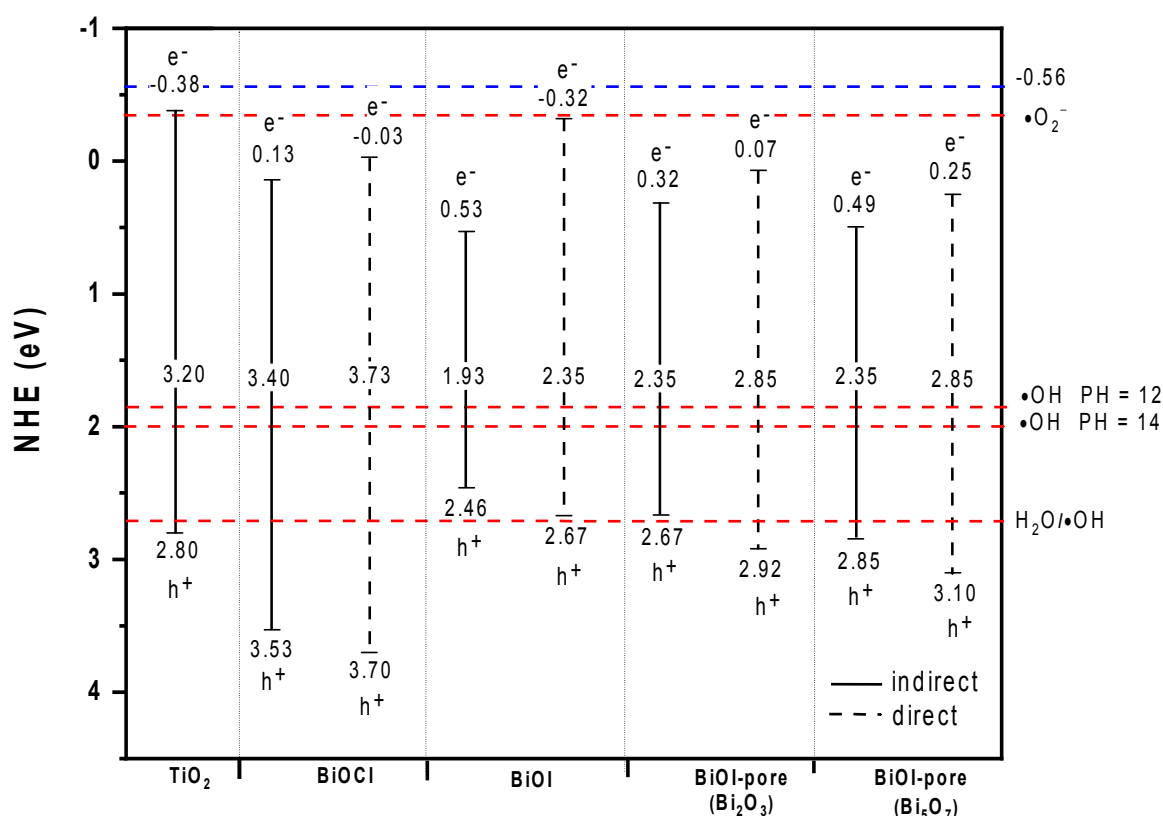


Figure 10. Cont.



**Figure 10.** Kubelka–Munk absorption curves of (a) pure-photocatalysts and (b) cement-based samples, (c) plots of  $(FRh\nu)^{1/2}$  vs. photon energy ( $h\nu$ ) for pure-photocatalysts (indirect transitions), and (d) plots of  $(FRh\nu)^2$  vs. photon energy ( $h\nu$ ) for pure-photocatalyst (direct transitions).



**Figure 11.** Schematic diagram of the band structure of  $\text{TiO}_2$ ,  $\text{BiOCl}$ ,  $\text{BiOI}$ , and phase transformation of  $\text{BiOI}$  into alkaline pH aqueous solution ( $\text{Bi}_2\text{O}_3$  and  $\text{Bi}_5\text{O}_7\text{I}$ ).

**Table 4.** Absolute electronegativity ( $\chi$ ), estimated band gap ( $E_g$ ) from DRS measurements and calculated  $E_{CV}$  and  $E_{VB}$  of  $\text{BiOX}$  photocatalysts.

Sample	$\chi$ (eV)	Indirect			Direct		
		$E_g$ (eV)	$E_{CB}$ (eV)	$E_{VB}$ (eV)	$E_g$ (eV)	$E_{CB}$ (eV)	$E_{VB}$ (eV)
$\text{BiOCl}$	6.33 <sup>a</sup>	3.40	0.13	3.53	3.73	−0.03	3.70
$\text{BiOI}$	5.99 <sup>a</sup>	1.93	0.53	2.46	2.35	−0.32	2.67
$\text{BiOI-pore (Bi}_2\text{O}_3)$	5.99 <sup>b</sup>	2.35	0.32	2.67	2.85	0.07	2.92
$\text{BiOI-pore (Bi}_5\text{O}_7\text{I)}$	6.17 <sup>c</sup>	2.35	0.49	2.85	2.85	0.25	3.10

<sup>a</sup> data were selected from the CRC handbook of chemistry and physics (87th edn, 2006–2007), <sup>b</sup> Electronegativity of  $\text{Bi}_2\text{O}_3$  [53], and <sup>c</sup> Electronegativity of  $\text{Bi}_5\text{O}_7\text{I}$  [44].

Concerning to the CB, theoretically, only  $\text{TiO}_2$  has sufficient energy potential to turn  $\text{O}_2$  to  $\bullet\text{O}_2^-$ . However, according to some researchers [54–56] under visible light irradiation, the photoinduced electrons of  $\text{BiOI}$  could jump to a reformed higher CB potential,  $\sim -0.56$  eV which is sufficient to reduce  $\text{O}_2$  to generate  $\bullet\text{O}_2^-$ . A similar band width photocatalytic mechanism also happens for  $\text{BiOCl}$ .

The presence of these CB bands of higher potential for the  $\text{BiOX}$  samples has been supported with the evaluation of the main reactive species as determined by Electron Paramagnetic Resonance (EPR) using an EMX micro 6/1 Bruker ESR spectrometer. The EPR measurements were carried out in neutral media and Dimethyl-1-pyrroline N-oxide (DMPO) was used to capture  $\bullet\text{OH}$  and  $\bullet\text{O}_2^-$ . Figure 12a demonstrates the generation of both  $\bullet\text{OH}$  and  $\bullet\text{O}_2^-$  photo-induced radicals over  $\text{BiOCl}$  pure oxides. For  $\text{BiOI}$ , it was possible to detect the signals of  $\bullet\text{O}_2^-$  and the absence of  $\bullet\text{OH}$  (Figure 12b). The production of  $\bullet\text{O}_2^-$  in both cases implies the existence of the reformed CB, and then, the promoted electrons can reduce oxygen and generate  $\bullet\text{O}_2^-$ . Likewise, the EPR results also corroborate the

theoretical VB position of the diagram in Figure 12. BiOCl is able to produce  $\text{OH}\bullet$  from the oxidation of  $\text{H}_2\text{O}$  molecule due to the energy position of their VB is much more negative than +2.72 eV. In contrast, the BiOI-VB position has not enough energy potential to oxidize water, and therefore  $\bullet\text{OH}$  is not detected.

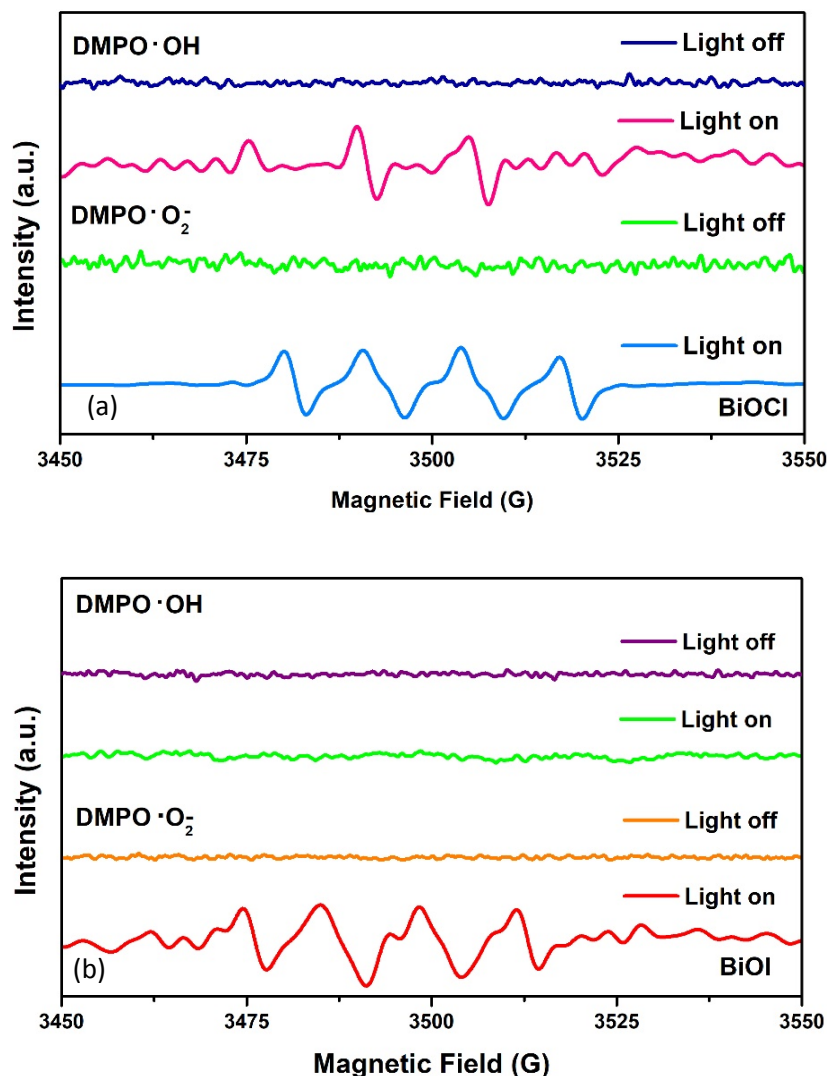


**Figure 12.** DMPO spin trapping Electron Paramagnetic Resonance (EPR) spectra for  $\text{DMPO}\text{-}\bullet\text{O}_2^-$  and  $\text{DMPO}\text{-}\bullet\text{OH}$  under visible light irradiation in neutral media with (a) BiOCl and (b) BiOI.

### 2.3. Photocatalytic Activity

The photocatalytic performance of cement/BiOX composites samples (BiOCl-cem and BiOI-cem) was evaluated by the removal of  $\text{NO}_x$  ( $\text{NO} + \text{NO}_2$ ) in gas phase under visible light.  $\text{TiO}_2$ -cem and Ref-cem were also evaluated under the same conditions. As expected, Ref-cem did not present any efficiency (data not included). The other three photocatalytic mortars showed photocatalytic activity. Figure 13 shows the summary of  $\text{NO}\text{-}\text{NO}_x$  removal and  $\text{NO}_2$  formed ( $\eta$ ) over the photocatalytic mortar samples under 30 min of visible-light irradiation. The highest conversion degree of  $\text{NO}$  (7.6%) was reached for BiOCl-cem followed by BiOI-cem and  $\text{TiO}_2$ -cem with results for  $\text{NO}$  removal quite similar. Provided that BiOCl-cem can only absorb a very small amount of visible light because of its wide band, its higher photocatalytic activity under visible light might be ascribed to the presence of oxygen vacancies, as in the case of  $\text{TiO}_2$ -cem [46,56,57]. Furthermore, the VB potential of BiOCl provides strong oxidation ability and the special crystal structures of BiOX whose  $[\text{Bi}_2\text{O}_2]^{2+}$  slabs and interleaved

halogen-ion layers are favorable to the formation of a self-built internal static electric field, which is very beneficial to the separation and migration of photo-induced electrons and holes [22,55,56,58]. The BiOI-cem sample showed low visible light activity (4.8%), even almost comparable with TiO<sub>2</sub>-cem (4.3%). Even though BiOI photocatalyst is suitable for visible-light excitation, its low NO removal activity can be ascribed to that its oxidation ability is much smaller, being the production of •OH only possible from the oxidation of OH<sup>-</sup>. In addition, it can be also ascribed to the phase transformation of BiOI to I-deficient bismuth oxyiodide compounds into the alkaline media of cementitious matrixes (Bi<sub>2</sub>O<sub>3</sub> and Bi<sub>5</sub>O<sub>7</sub>I). Although these compounds show a VB potential more positive than pure BiOI, their absorption of visible light decreases considerably (see Figure 10b).

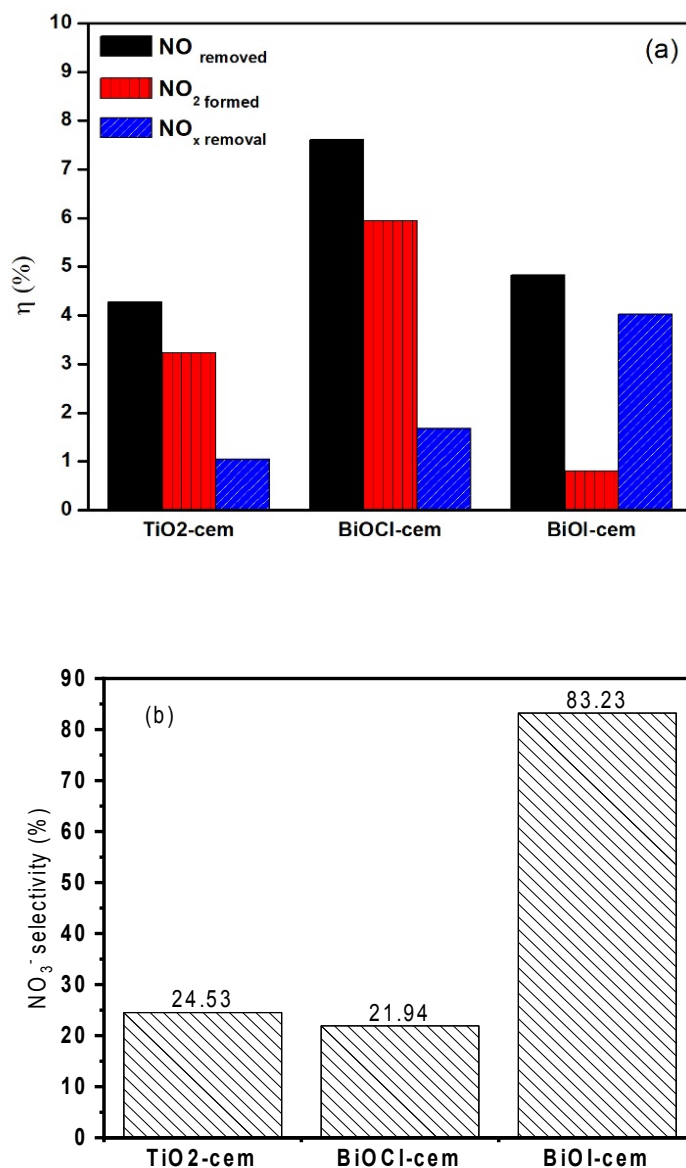


**Figure 13.** (a) NO-NO<sub>x</sub> removed and NO<sub>2</sub> formed efficiency (%) and (b) nitrate selectivity of photocatalyst/cement composites.

It is remarkable the higher nitrate selectivity of the BiOI-cem sample and the undesirable production of NO<sub>2</sub> from the other two samples. This is a very important aspect as being NO<sub>2</sub> more toxic than NO, the global effect would be negative for the environment and public health. Thus, nitrate selectivity has to be considered when evaluating photocatalyst performance [59]. The mechanism of NO<sub>x</sub> removal is very complex, and it is not completely understood yet. There are several theories

about factors that affect selectivity. The possible causes are out of the scope of this paper and they will be studied next by the authors.

### 3. Experimental

#### 3.1. Synthesis of BiOX (X = Cl and I) Powders

BiOCl oxide was prepared by co-precipitation synthesis starting from bismuth (III) nitrate pentahydrate ( $\text{Bi}(\text{NO}_3)_3 \cdot 5\text{H}_2\text{O}$ , Sigma Aldrich, 98%), acetic acid ( $\text{C}_2\text{H}_4\text{O}_2$ , Fermont, 99.8%), ethylenediaminetetraacetic acid disodium salt (EDTA, DEQ, 99.7%) and potassium chloride (KCl, DEQ, 99.5%). All reagents were directly used as received without any additional purification. In a typical procedure, 0.1 M solution of  $\text{Bi}(\text{NO}_3)_3 \cdot 5\text{H}_2\text{O}$  in acetic acid (9% V/V) was prepared using magnetic stirring. Separately, solutions 0.1 M of EDTA and potassium chloride dissolved in deionized water were also prepared. In the first step, 40 mL of EDTA solution and 100 mL  $\text{Bi}(\text{NO}_3)_3 \cdot 5\text{H}_2\text{O}$  solution were mixed by dropping. After 30 min of continuous stirring, 60 mL of KCl solution was added drop by drop and then the resulting mixture was continuously stirred for 24 h at room temperature. After the reaction time, the powder was separated by filtration and washed three times with deionized water and two times with ethanol. Finally, the product was dried in an electrical oven at 70 °C for 24 h.

The synthesis of BiOI involved the preparation of 10 mL of nitrate bismuth and potassium iodide 0.1 M solutions (KI, DEQ, 99.5%) in ethylene glycol ( $\text{C}_2\text{H}_6\text{O}_2$ , Fermont, 99.9%). In a first step, KI solution was added drop by drop in  $\text{Bi}(\text{NO}_3)_3 \cdot 5\text{H}_2\text{O}$  solution with vigorous stirring. The resulting solution was transferred into a 30-mL quartz tube that was sealed with a silicone septum and placed into a Monowave 300 Anton Paar microwave reactor. Then, the mixture was heated to 125 °C within 3 min and kept at this temperature for 15 min with continuous magnetic stirring at 800 rpm. After being cooled down to 70 °C, the powder formed was filtered and washed three times with deionized water and two times with ethanol. Finally, the product was dried in an oven at 70 °C for 24 h.

#### 3.2. Preparation of Cement-Based Samples

All the mortar mixes were prepared according to UNE-EN-196-1 with a cement:sand ratio of 1:3 using Portland cement BLI 52.5 R. The elemental composition of cement in wt.%, determined by X-ray fluorescence (XRF) was (loss of ignition 2.74): CaO: 66.07,  $\text{SiO}_2$ : 20.67,  $\text{Al}_2\text{O}_3$ : 4.18,  $\text{Fe}_2\text{O}_3$ : 0.27, MgO: 0.44,  $\text{SO}_3$ : 2.90,  $\text{P}_2\text{O}_5$ : 0.06,  $\text{K}_2\text{O}$ : 0.6, Cl 0.02 and  $\text{TiO}_2$ : 0.24. BiOCl and BiOI were incorporated into the mortar mixture at 10 w% by cement. For comparative purposes, a mixture with commercial  $\text{TiO}_2$  (10 w%, Aerioxide<sup>®</sup>  $\text{TiO}_2$ -P25 from Evonik 75% anatase and 25% rutile) and another mixture without photocatalyst were also prepared. The obtained samples were labeled as, BiOCl-cem, BiOI-cem,  $\text{TiO}_2$ -cem, and Ref-cem, respectively. The water-to-cement ratio was kept at 0.58 in all photocatalytic mixtures and 0.50 for the reference sample. The samples were cured in an environmental chamber ( $25 \pm 2$  °C and RH > 95%) for 28 days.

#### 3.3. Physicochemical Characterization

##### 3.3.1. Photocatalysts Powders

The crystalline phases of as-synthesized BiOX photocatalysts were characterized by X-ray powder diffraction (XRD) in a Bruker D8 Advance diffractometer with radiation of  $\text{CuK}_\alpha$  (40 kV, 30 mA). The morphology was characterized by scanning electron microscopy (BSE-SEM) using a Hitachi S-4800 microscope.

Sedimentation trials of photocatalysts using 4 mL of the synthetic solution of the alkaline-like pore of mortars according to previous works [38,60] and the same volume of every catalyst were carried out based on the described procedure by Folli et al. [38]. The composition of the pore-cement solution was 48.9 mmol/L  $\text{Na}_2\text{SO}_4$ , 21.2 mmol/L  $\text{Ca}(\text{OH})_2$ , 106.2 mmol/L KOH and 37 mmol/L  $\text{K}_2\text{SO}_4$  leading to a pH of 12.87.

### 3.3.2. Cement-Based Materials

Fresh state and hardened characteristics of cement-based materials were evaluated following the procedure described in the UNE-EN-1015-7 standard. Compressive strength tests were carried out on the  $4 \times 4 \times 16$  cm cubic specimens according to UNE-EN-1015-11 standard. Electrical resistivity tests were carried out in specimens with dimensions of  $40 \times 40 \times 160$  mm using the direct method with an Escort ELC-131 D equipment [61].

XRD and BSE-SEM analysis were performed in a Bruker Advance-D8 diffractometer and a Hitachi S-4800 scanning electron microscope, respectively. TG-TDA measurements were performed under  $N_2$  gas with a heating rate of  $10 \text{ }^\circ\text{C}/\text{min}$  using an SDT Q600 equipment from room temperature to  $1000 \text{ }^\circ\text{C}$ . The specific surface area was measured by  $N_2$  physisorption through the Brunauer–Emmett–Teller (BET) method, and the porosity and pore size distribution of the mortars were determined by means of mercury intrusion porosimetry (MIP) using an AutoPore IV 9500 Micromeritics.

### 3.4. Optical Properties

Shimadzu UV-VIS spectrophotometer model UV-2600 was used to obtain the diffuse reflectance spectra (DRS) of pure photocatalysts and cement-based samples. The reflectance values were converted to absorption data according to the Kubelka–Munk method [46].

In order to obtain the band edge ( $E_g$ ) values of photocatalyst samples, the Kubelka–Munk optical absorption coefficients  $[F(R)]$  were plotted using Tauc's relation (Equation (3))

$$F(R)hv = (hv - E_g)^n \quad (3)$$

where  $F(R)$ ,  $hv$  and  $E_g$  are the Kubelka–Munk optical absorption coefficient, energy of the incident photon, and band gap energy, respectively. Among them,  $n$  depends on the characteristics of the transition in a semiconductor (i.e.,  $n = 2$  for indirect transition or  $n = 1/2$  for direct transition) [46].

### 3.5. Photocatalytic Performance

The photocatalytic performance of the mortars was evaluated measuring the removal of  $NO_x$  ( $NO + NO_2$ ) in gas phase under visible-light irradiation in a continuous flow reactor based on the requirements of ISO standard 22197-1:2007. As inlet gas, nitric oxide (NO) diluted in air with a concentration of  $1000 \pm 50$  ppb and flow rate controlled at  $3 \text{ L}/\text{min}$  was used. After reaching the adsorption-desorption equilibrium of NO (30 min), the lamps were turned on for 30 min. Two fluorescent lamps Philips-MASTER TL-D Super 80 15 W (16,000 Lux). The lamp spectra are given in Figure 14. The relative humidity was maintained at about  $50\% \pm 5\%$  at a temperature of  $25 \text{ }^\circ\text{C}$ . A normalized test piece surface area of  $49.25 \text{ cm}^2$  was used. The concentration of NO and intermediate products,  $NO_2$ , was measured with a chemiluminescent  $NO_x$  analyzer (AC32M Environmental S.A.). Efficiencies ( $\eta$ ) for NO removed,  $NO_2$  formed, and total  $NO_x$  removal were determined separately according to Equations (4)–(6).

$$\eta NO_{removed} = \frac{NO_{in} - NO_{out}}{NO_{in}} \times 100 \quad (4)$$

$$\eta NO_{2formed} = \frac{NO_{2out} - NO_{2in}}{NO_{2out}} \times 100 \quad (5)$$

$$\eta NO_{xremoval} = \eta NO_{removed} - \eta NO_{2formed} \quad (6)$$

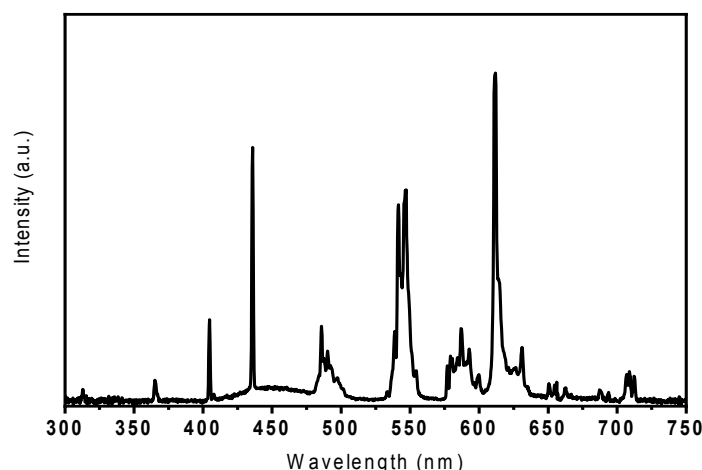


Figure 14. Spectral irradiance profile of the fluorescent light source used.

Finally, the  $\text{NO}_3^-$  selectivity (i.e., the ratio of  $\text{NO}$  converted to nitrates) was derived according to Equation (7).

$$\text{NO}_3^- \text{ Selectivity}(\%) = \frac{\eta \text{NO}_{\text{Xremoval}}}{\eta \text{NO}_{\text{removed}}} \times 100 \quad (7)$$

#### 4. Conclusions

Photocatalytic mortars were prepared by the addition of  $\text{BiOX}$  ( $X = \text{Cl}$  and  $\text{I}$ ) and  $\text{TiO}_2$  to study their feasibility as visible-light-driven photocatalytic construction materials. From this research, the following conclusions can be derived:

- $\text{BiOCl}$  and  $\text{BiOI}$  are particles of spherical shape with a flower-like morphology and micrometric size, which reduces the concerns about the possible unwanted effects of the use of nanoparticles.
- The presence of the reformed CB with higher reduction potential in the  $\text{BiOX}$ . Therefore, promoted electrons can reduce oxygen and generate superoxide radicals. The position of the VB of  $\text{BiOCl}$  allows the oxidation of  $\text{H}_2\text{O}$  to form  $\bullet\text{OH}$ . In the case of  $\text{BiOI}$  in neutral media, VB has not the potential to oxidize water and therefore,  $\bullet\text{OH}$  is not detected.
- In alkaline media,  $\text{TiO}_2$  forms flocculated sediment. Meanwhile,  $\text{BiOI}$  presents intermediate behavior and for  $\text{BiOCl}$  no flocculation occurred. The differences can be attributed to particle size.
- There is a chemical interaction between the  $\text{BiOI}$  and the alkaline aqueous phase of the cement, which leads to the formation, among others, of  $\text{Bi}_2\text{O}_3$  and  $\text{Bi}_5\text{O}_7\text{I}$ . These compounds show a lower visible light absorption capacity than  $\text{BiOI}$ .
- The interaction between  $\text{BiOX}$  photocatalysts and cement matrix does not appear to adversely affect the inherent properties of cement-based materials.  $\text{TiO}_2$  results in drier samples, while  $\text{BiOX}$  induces more fluid behavior. Only  $\text{TiO}_2$  acts as a filler to refine the cement pore structure.
- The  $\text{BiOCl}$ -cem sample showed higher photocatalytic activity than the other samples in terms of  $\text{NO}$  removal.  $\text{BiOI}$ -cem showed a nitrate selectivity of  $\sim 83\%$ , which is much higher than  $\text{TiO}_2$ -cem ( $\sim 24\%$ ) and  $\text{BiOCl}$ -cem ( $\sim 22\%$ ). The lower amount of  $\text{NO}_2$  produced by  $\text{BiOI}$ -cem results in the highest  $\text{NO}_x$  removal efficiency. These results make its use a safer and environmentally sustainable option.

**Author Contributions:** Conceptualized and designed the experiments, M.C. and A.M.-d.l.C.; contributed reagents/materials/analysis tools, M.C. and A.M.-d.l.C.; investigation, M.Y.N.-N. and E.J.-R.; performed the experiments, M.Y.N.-N. and M.G.; analyzed the data, M.Y.N.-N., E.J.-R., M.C. and A.M.-d.l.C.; writing—original draft M.Y.N.-N. and E.J.-R.; writing—review & editing M.Y.N.-N., E.J.-R., M.C. and A.M.-d.l.C. All authors have read and agreed to the published version of the manuscript.

**Funding:** This research received no external funding.

**Acknowledgments:** We wish to thank to CONACYT for its invaluable financial support through scholarship to Magaly Yajaira Nava Núñez.

**Conflicts of Interest:** The authors declare no conflict of interest.

## References

1. Chen, J.; Poon, C. Photocatalytic construction and building materials: From fundamentals to applications. *Build. Environ.* **2009**, *44*, 1899–1906. [CrossRef]
2. Jimenez-Relinque, E.; Rodriguez-Garcia, J.R.; Castillo, A.; Castellote, M. Characteristics and efficiency of photocatalytic cementitious materials: Type of binder, roughness and microstructure. *Cem. Concr. Res.* **2015**, *71*, 124–131. [CrossRef]
3. Guo, S.; Wu, Z.; Zhao, W. TiO<sub>2</sub>-based building materials: Above and beyond traditional applications. *Chin. Sci. Bull.* **2009**, *54*, 1137–1142. [CrossRef]
4. Laplaza, A.; Jimenez-Relinque, E.; Campos, J.; Castellote, M. Photocatalytic behavior of colored mortars containing TiO<sub>2</sub> and iron oxide based pigments. *Constr. Build. Mater.* **2017**, *144*, 300–310. [CrossRef]
5. Sapiña, M.; Jimenez-Relinque, E.; Castellote, M. Controlling the levels of airborne pollen: Can heterogeneous photocatalysis help? *Environ. Sci. Technol.* **2013**, *47*, 11711–11716. [CrossRef] [PubMed]
6. Jimenez-Relinque, E.; Sapiña, M.; Nevshupa, R.; Roman, E.; Castellote, M. Photocatalytic decomposition of pollen allergenic extracts of *Cupressus arizonica* and *Platanus hybrida*. *Chem. Eng. J.* **2016**, *286*, 560–570. [CrossRef]
7. Jiménez-Relinque, E.; Hingorani, R.; Rubiano, F.; Grande, M.; Castillo, Á.; Castellote, M. In situ evaluation of the NO<sub>x</sub> removal efficiency of photocatalytic pavements: Statistical analysis of the relevance of exposure time and environmental variables. *Environ. Sci. Pollut. Res.* **2019**, 1–8. [CrossRef]
8. Bengtsson, N.; Castellote, M. Heterogeneous photocatalysis on construction materials: Effect of catalyst properties on the efficiency for degrading NO<sub>x</sub> and self cleaning. *Mater. Constr.* **2014**, *64*, 1–17. [CrossRef]
9. Ai, Z.; Ho, W.; Lee, S.; Zhang, L. Efficient photocatalytic removal of NO in indoor air with hierarchical bismuth oxybromide nanoplate microspheres under visible light. *Environ. Sci. Technol.* **2009**, *43*, 4143–4150. [CrossRef]
10. Dong, F.; Zhao, Z.; Sun, Y.; Zhang, Y.; Yan, S.; Wu, Z. An Advanced Semimetal-Organic Bi Spheres-g-C<sub>3</sub>N<sub>4</sub> Nanohybrid with SPR-Enhanced Visible-Light Photocatalytic Performance for NO Purification. *Environ. Sci. Technol.* **2015**, *49*, 12432–12440. [CrossRef]
11. Doustkhah, E.; Ide, Y. Microporous Layered Silicates: Old but New Microporous Materials. *New J. Chem.* **2020**, 1–30. [CrossRef]
12. Yang, X.; Yang, D.; Zhu, H.; Liu, J.; Martins, W.N.; Frost, R.; Daniel, L.; Shen, Y. Mesoporous structure with size controllable anatase attached on silicate layers for efficient photocatalysis. *J. Phys. Chem. C* **2009**, *113*, 8243–8248. [CrossRef]
13. Xiao, F.X.; Miao, J.; Liu, B. Layer-by-layer self-assembly of CdS quantum dots/graphene nanosheets hybrid films for photoelectrochemical and photocatalytic applications. *J. Am. Chem. Soc.* **2014**, *136*, 1559–1569. [CrossRef] [PubMed]
14. Liao, G.; Chen, S.; Quan, X.; Yu, H.; Zhao, H. Graphene oxide modified g-C<sub>3</sub>N<sub>4</sub> hybrid with enhanced photocatalytic capability under visible light irradiation. *J. Mater. Chem.* **2012**, *22*, 2721–2726. [CrossRef]
15. Niu, P.; Zhang, L.; Liu, G.; Cheng, H.M. Graphene-like carbon nitride nanosheets for improved photocatalytic activities. *Adv. Funct. Mater.* **2012**, *22*, 4763–4770. [CrossRef]
16. De la Peña-Benítez, P.R.; García-Santos, A.; Santonja, R.; Sapiña, M.; Jiménez-Relinque, E.; Castellote, M.; Sánchez-Cifuentes, M. Evaluación ambiental de pinturas al agua para exteriores de los edificios modificadas con óxido de grafeno. *Superficies y vacío* **2016**, *29*, 105–111. Available online: <http://journal.smctsm.org.mx/index.php/SyV/article/viewFile/85/55> (accessed on 16 January 2020).
17. Takata, T.; Furumi, Y.; Shinohara, K.; Tanaka, A.; Hara, M.; Kondo, J.N.; Domen, K. Photocatalytic Decomposition of Water on Spontaneously Hydrated Layered Perovskites. *Chem. Mater.* **1997**, *9*, 1063–1064. [CrossRef]

18. Sano, T.; Tsutsui, S.; Koike, K.; Hirakawa, T.; Teramoto, Y.; Negishi, N.; Takeuchi, K. Activation of graphitic carbon nitride (g-C<sub>3</sub>N<sub>4</sub>) by alkaline hydrothermal treatment for photocatalytic NO oxidation in gas phase. *J. Mater. Chem. A* **2013**, *1*, 6489–6496. [[CrossRef](#)]
19. Cao, S.; Low, J.; Yu, J.; Jaroniec, M. Polymeric Photocatalysts Based on Graphitic Carbon Nitride. *Adv. Mater.* **2015**, *27*, 2150–2176. [[CrossRef](#)]
20. Mohapatra, L.; Parida, K. A review on the recent progress, challenges and perspective of layered double hydroxides as promising photocatalysts. *J. Mater. Chem. A* **2016**, *4*, 10744–10766. [[CrossRef](#)]
21. Ye, L.; Su, Y.; Jin, X.; Xie, H.; Zhang, C. Recent advances in BiOX (X = Cl, Br and I) photocatalysts: Synthesis, modification, facet effects and mechanisms. *Environ. Sci. Nano* **2014**, *1*, 90–112. [[CrossRef](#)]
22. Yang, Y.; Zhang, C.; Lai, C.; Zeng, G.; Huang, D.; Cheng, M.; Wang, J.; Chen, F.; Zhou, C.; Xiong, W. BiOX (X = Cl, Br, I) photocatalytic nanomaterials: Applications for fuels and environmental management. *Adv. Colloid Interface Sci.* **2018**, *254*, 76–93. [[CrossRef](#)]
23. Ou, M.; Dong, F.; Zhang, W.; Wu, Z. Efficient visible light photocatalytic oxidation of NO in air with band-gap tailored (BiO)<sub>2</sub>CO<sub>3</sub>-BiOI solid solutions. *Chem. Eng. J.* **2014**, *255*, 650–658. [[CrossRef](#)]
24. Lv, J.; Hu, Q.; Cao, C.; Zhao, Y. Modulation of valence band maximum edge and photocatalytic activity of BiOX by incorporation of halides. *Chemosphere* **2018**, *191*, 427–437. [[CrossRef](#)] [[PubMed](#)]
25. Dong, F.; Sun, Y.; Fu, M.; Wu, Z.; Lee, S.C. Room temperature synthesis and highly enhanced visible light photocatalytic activity of porous BiOI/BiOCl composites nanoplates microflowers. *J. Hazard. Mater.* **2012**, *219*, 26–34. [[CrossRef](#)] [[PubMed](#)]
26. Wu, X.; Zhang, K.; Zhang, G.; Yin, S. Facile preparation of BiOX (X = Cl, Br, I) nanoparticles and up-conversion phosphors/BiOBr composites for efficient degradation of NO gas: Oxygen vacancy effect and near infrared light responsive mechanism. *Chem. Eng. J.* **2017**, *325*, 59–70. [[CrossRef](#)]
27. Jiang, G.; Li, X.; Lan, M.; Shen, T.; Lv, X.; Dong, F.; Zhang, S. Monodisperse bismuth nanoparticles decorated graphitic carbon nitride: Enhanced visible-light-response photocatalytic NO removal and reaction pathway. *Appl. Catal. B Environ.* **2017**, *205*, 532–540. [[CrossRef](#)]
28. Mera, A.C.; la Cruz, A.M.; Pérez-Tijerina, E.; Meléndrez, M.F.; Valdés, H. Nanostructured BiOI for air pollution control: Microwave-assisted synthesis, characterization and photocatalytic activity toward NO transformation under visible light irradiation. *Mater. Sci. Semicond. Process.* **2018**, *88*, 20–27. [[CrossRef](#)]
29. Zhang, W.; Zhang, Q.; Dong, F. Visible-light photocatalytic removal of NO in air over BiOX (X = Cl, Br, I) single-crystal nanoplates prepared at room temperature. *Ind. Eng. Chem. Res.* **2013**, *52*, 6740–6746. [[CrossRef](#)]
30. Jimenez-Relinque, E.; Castellote, M. Quantification of hydroxyl radicals on cementitious materials by fluorescence spectrophotometry as a method to assess the photocatalytic activity. *Cem. Concr. Res.* **2015**, *74*, 108–115. [[CrossRef](#)]
31. Yang, L.; Hakki, A.; Wang, F.; Macphee, D.E. Different Roles of Water in Photocatalytic DeNO<sub>x</sub> Mechanisms on TiO<sub>2</sub>: Basis for Engineering Nitrate Selectivity? *ACS Appl. Mater. Interfaces* **2017**, *9*, 17034–17041. [[CrossRef](#)] [[PubMed](#)]
32. Ohko, Y.; Nakamura, Y.; Fakuda, A.; Matsuzawa, S.; Takeuchi, K. Photocatalytic oxidation of nitrogen monoxide using TiO<sub>2</sub> thin films under continuous UV light illumination. *J. Photochem. Photobiol. A Chem.* **2008**, *112*, 10502–10508. [[CrossRef](#)]
33. Wang, D.; Hou, P.; Yang, P.; Cheng, X. BiOBr@SiO<sub>2</sub> flower-like nanospheres chemically-bonded on cement-based materials for photocatalysis. *Appl. Surf. Sci.* **2018**, *430*, 539–548. [[CrossRef](#)]
34. Tallapally, V.; Nakagawara, T.A.; Demchenko, D.O.; Özgür, Ü.; Arachchige, I.U. Ge<sub>1-x</sub>Sn<sub>x</sub> alloy quantum dots with composition-tunable energy gaps and near-infrared photoluminescence. *Nanoscale* **2018**, *10*, 20296–20305. [[CrossRef](#)] [[PubMed](#)]
35. Borchert, H.; Shevchenko, E.V.; Robert, A.; Mekis, I.; Kornowski, A.; Grübel, G.; Weller, H. Determination of nanocrystal sizes: A comparison of TEM, SAXS, and XRD studies of highly monodisperse CoPt<sub>3</sub> particles. *Langmuir* **2005**, *21*, 1931–1936. [[CrossRef](#)] [[PubMed](#)]
36. Henle, J.; Simon, P.; Frenzel, A.; Scholz, S.; Kaskel, S. Nanosized BiOX (X = Cl, Br, I) particles synthesized in reverse microemulsions. *Chem. Mater.* **2007**, *19*, 366–373. [[CrossRef](#)]
37. Henle, J.; Kaskel, S. Preparation of photochromic transparent BiOX (X = Cl, I)/PLA nanocomposite materials via microemulsion polymerization. *J. Mater. Chem.* **2007**, *17*, 4964–4971. [[CrossRef](#)]

38. Folli, A.; Pochard, I.; Nonat, A.; Jakobsen, U.H.; Shepherd, A.M.; Macphee, D.E. Engineering Photocatalytic Cements: Understanding TiO<sub>2</sub> Surface Chemistry to Control and Modulate Photocatalytic Performances. *J. Am. Ceram. Soc.* **2010**, *93*, 3360–3369. [[CrossRef](#)]
39. Shaw, D.J. *Introduction to Colloid and Surface Chemistry*; Butterworths: Waltham, MA, USA, 1968; p. 212.
40. Sun, S.; Wang, W.; Zhang, L.; Zhou, L.; Yin, W.; Meng, S. Bi<sub>5</sub>O<sub>7</sub>Br and its structural relation to α-Bi<sub>5</sub>O<sub>7</sub>I. *Environ. Sci. Technol.* **2009**, *43*, 2005–2010. [[CrossRef](#)]
41. Wu, G.; Zhao, Y.; Li, Y.; Ma, H.; Zhao, J. pH-dependent synthesis of iodine-deficient bismuth oxyiodide microstructures: Visible-light photocatalytic activity. *J. Colloid Interface Sci.* **2018**, *510*, 228–236. [[CrossRef](#)]
42. Long, M.; Hu, P.; Wu, H.; Chen, Y.; Tan, B.; Cai, W. Understanding the composition and electronic structure dependent photocatalytic performance of bismuth oxyiodides. *J. Mater. Chem. A* **2015**, *3*, 5592–5598. [[CrossRef](#)]
43. Cote, P.; Gilliam, M. *Environmental Aspects of Stabilization and Solidification of Hazardous and Radioactive Wastes*; ASTM International: West Conshohocken, PA, USA, 1989; p. 1033.
44. Yang, J.; Xu, L.; Liu, C.; Xie, T. Preparation and photocatalytic activity of porous Bi<sub>5</sub>O<sub>7</sub>I nanosheets. *Appl. Surf. Sci.* **2014**, *319*, 265–271. [[CrossRef](#)]
45. Zhang, J.; Yu, J.; Zhang, Y.; Li, Q.; Gong, J.R. Visible light photocatalytic H<sub>2</sub>-production activity of CuS/ZnS porous nanosheets based on photoinduced interfacial charge transfer. *Nano Lett.* **2011**, *11*, 4774–4779. [[CrossRef](#)]
46. Jimenez-Relinque, E.; Llorente, I.; Castellote, M. TiO<sub>2</sub> cement-based materials: Understanding optical properties and electronic band structure of complex matrices. *Catal. Today* **2017**, *287*, 203–209. [[CrossRef](#)]
47. Galan, I.; Andrade, C.; Castellote, M. Thermogravimetric analysis for monitoring carbonation of cementitious materials: Uptake of CO<sub>2</sub> and deepening in C-S-H knowledge. *J. Anal. Calorim.* **2012**, *110*, 309–319. [[CrossRef](#)]
48. Yu, C.; Fan, C.; Yu, J.C.; Zhou, W.; Yang, K. Preparation of bismuth oxyiodides and oxides and their photooxidation characteristic under visible/UV light irradiation. *Mater. Res. Bull.* **2011**, *46*, 140–146. [[CrossRef](#)]
49. Tallapally, V.; Esteves, R.J.A.; Nahar, L.; Arachchige, I.U. Multivariate Synthesis of Tin Phosphide Nanoparticles: Temperature, Time, and Ligand Control of Size, Shape, and Crystal Structure. *Chem. Mater.* **2016**, *28*, 5406–5414. [[CrossRef](#)]
50. Nadtochenko, V.; Denisov, N.; Gorenberg, A.; Kozlov, Y.; Chubukov, P.; Rengifo, J.A.; Pulgarin, C.; Kiwi, J. Correlations for photocatalytic activity and spectral features of the absorption band edge of TiO<sub>2</sub> modified by thiourea. *Appl. Catal. B Environ.* **2009**, *91*, 460–469. [[CrossRef](#)]
51. Singla, P.; Pandey, O.P.; Singh, K. Study of photocatalytic degradation of environmentally harmful phthalate esters using Ni-doped TiO<sub>2</sub> nanoparticles. *Int. J. Environ. Sci. Technol.* **2015**, *13*, 849–856. [[CrossRef](#)]
52. Li, Y.; Wang, J.; Yao, H.; Dang, L.; Li, Z. Chemical etching preparation of BiOI/Bi<sub>2</sub>O<sub>3</sub> heterostructures with enhanced photocatalytic activities. *Catal. Commun.* **2011**, *12*, 660–664. [[CrossRef](#)]
53. Yi, S.; Yue, X.; Xu, D.; Liu, Z.; Zhao, F.; Wang, D.; Lin, Y. Study on photogenerated charge transfer properties and enhanced visible-light photocatalytic activity of p-type Bi<sub>2</sub>O<sub>3</sub>/n-type ZnO heterojunctions. *New J. Chem.* **2015**, *39*, 2917–2924. [[CrossRef](#)]
54. Huang, H.; Han, X.; Li, X.; Wang, S.; Chu, P.K.; Zhang, Y. Fabrication of multiple heterojunctions with tunable visible-light-active photocatalytic reactivity in BiOBr–BiOI full-range composites based on microstructure modulation and band structures. *ACS Appl. Mater. Interfaces* **2015**, *7*, 482–492. [[CrossRef](#)] [[PubMed](#)]
55. Zhang, K.L.; Liu, C.M.; Huang, F.Q.; Zheng, C.; Wang, W.D. Study of the electronic structure and photocatalytic activity of the BiOCl photocatalyst. *Appl. Catal. B Environ.* **2006**, *68*, 125–129. [[CrossRef](#)]
56. Choudhury, B.; Choudhury, A. Oxygen defect dependent variation of band gap, Urbach energy and luminescence property of anatase, anatase-rutile mixed phase and of rutile phases of TiO<sub>2</sub> nanoparticles. *Phys. E Low-Dimens. Syst. Nanostruct.* **2014**, *56*, 364–371. [[CrossRef](#)]
57. Smith, A.M.; Nie, S. Semiconductor nanocrystals: Structure, properties, and band gap engineering. *Acc. Chem. Res.* **2010**, *43*, 190–200. [[CrossRef](#)]
58. Jiang, J.; Zhang, X.; Sun, P.; Zhang, L. ZnO/BiOI heterostructures: Photoinduced charge-transfer property and enhanced visible-light photocatalytic activity. *J. Phys. Chem. C* **2011**, *115*, 20555–20564. [[CrossRef](#)]
59. Bloh, J.Z.; Dillert, R.; Bahnemann, D.W. Ruthenium-modified zinc oxide, a highly active vis-photocatalyst: The nature and reactivity of photoactive centres. *Phys. Chem. Chem. Phys.* **2014**, *16*, 5833–5845. [[CrossRef](#)]

60. Houst, Y.F.; Bowen, P.; Perche, F.; Kauppi, A.; Borget, P.; Galmiche, L.; le Meins, J.; Lafuma, F.; Flatt, R.J.; Schober, I.; et al. Design and function of novel superplasticizers for more durable high performance concrete (superplast project). *Cem. Concr. Res.* **2008**, *38*, 1197–1209. [[CrossRef](#)]
61. Castellote, M.; Andrade, C.; Alonso, M.C. Standardization, to a Reference of 25 °C, of Electrical Resistivity for Mortars and Concretes in Saturated or Isolated Conditions. *ACI Mater. J.* **2003**, *99*, 119–128.



© 2020 by the authors. Licensee MDPI, Basel, Switzerland. This article is an open access article distributed under the terms and conditions of the Creative Commons Attribution (CC BY) license (<http://creativecommons.org/licenses/by/4.0/>).